SCIENTIFIC REPORTS

OPEN

SUBJECT AREAS:
THEORY AND COMPUTATION
MECHANICAL ENGINEERING

Received
19 May 2014

Accepted
14 July 2014

Published
7 August 2014

Correspondence and requests for materials should be addressed to H.J. (hanqing.jiang@asu.edu)

Origami based Mechanical Metamaterials

Cheng Lv[1], Deepakshyam Krishnaraju[1], Goran Konjevod[1], Hongyu Yu[2] & Hanqing Jiang[1]

[1]School for Engineering of Matter, Transport and Energy, Arizona State University, Tempe, AZ 85287 (USA), [2]School of Earth and Space Exploration, School of Electrical, Computer and Energy Engineering, Arizona State University, Tempe, AZ 85287 (USA).

We describe mechanical metamaterials created by folding flat sheets in the tradition of origami, the art of paper folding, and study them in terms of their basic geometric and stiffness properties, as well as load bearing capability. A periodic Miura-ori pattern and a non-periodic Ron Resch pattern were studied. Unexceptional coexistence of positive and negative Poisson's ratio was reported for Miura-ori pattern, which are consistent with the interesting shear behavior and infinity bulk modulus of the same pattern. Unusually strong load bearing capability of the Ron Resch pattern was found and attributed to the unique way of folding. This work paves the way to the study of intriguing properties of origami structures as mechanical metamaterials.

Mechanical metamaterials, the man-made materials with mechanical properties mainly defined by their structures instead of the properties of each component, recently have attracted great attention[1–4]. Origami, creating three-dimensional (3D) structures from two-dimensional (2D) sheets through a process of folding along creases, provides an interesting source for designing mechanical metamaterials and has been transformed by mathematicians, scientists, and engineers to utilize the folded objects' deformability and compactness in applications ranging from space exploration (e.g., a foldable telescope lens[5]), to automotive safety (e.g., airbags[6]), biomedical devices (e.g., heart stent[7]), and extremely foldable and stretchable electronics[8,9]. Notable progress has been made in the area of origami theory including tree theory[10] and its corresponding computer program[11], folding along creases[12–14], and geometric mechanics of a periodic origami pattern[15]. Among classes of origami patterns, a particular one, namely rigid origami, in which the faces between the creases remain rigid during folding/unfolding and only the creases deform, is different from most origami patterns that require faces bending or partial crumpling to make many-step folds. Idealized rigid origami possesses one of the most obvious advantages of origami in terms of deformation, i.e., the deformation is completely realized by the folding/unfolding at the creases and does not involve any deformation at the rigid faces[4]. The geometric characteristics, such as the necessary condition around a single vertex for rigid origami[16,17] have been studied, and a computer simulator for rigid origami[18] exists. There have also been made limited efforts to study the structural characteristics of one particular rigid origami, namely Miura-ori[19], as a mechanical metamaterial, with the main focus on the negative Poisson's ratio[15,20], though these properties can be more rigorously examined. It is noticed that the existing studies are mainly focused on periodic origami patterns (e.g., Miura-ori); however, non-periodic origami patterns as mechanical metamaterials have not gained attention yet, partially due to the difficulties in theoretical analysis and modeling. To span a much wider spectrum of using rigid origami as mechanical metamaterials, we report a systematic study of two rigid origami folding patterns, not only the periodic Miura-ori but also a non-periodic Ron Resch folding[21] using combined analytical and numerical approaches. Specifically, we rigorously address the commonly mistaken in-plane Poisson's ratio of Miura-ori, which was believed to be always negative but we show here that it can be positive as well, and its physical interpretation. The ubiquitous non-local interactions between vertices of rigid origami patterns are captured through a non-local finite element approach and the compressive buckling resistance of a Ron Resch tube is studied, which inspires a theoretical and experimental study of the load bearing capability of the Ron Resch pattern. The result witnesses the superb load bearing capability of this Ron Resch pattern. Based on the approaches in this paper, mechanical properties of different rigid origami patterns, both periodic and non-periodic ones, can be readily studied.

Results

Unit cell and the whole pattern of a Miura-ori. Figure 1a illustrates a Miura-ori (n_1, n_2) in its folded state, containing n_1 (=11) vertices in x_1 direction and n_2 (=11) vertices in x_2 direction, with x_3 as the out-of-plane

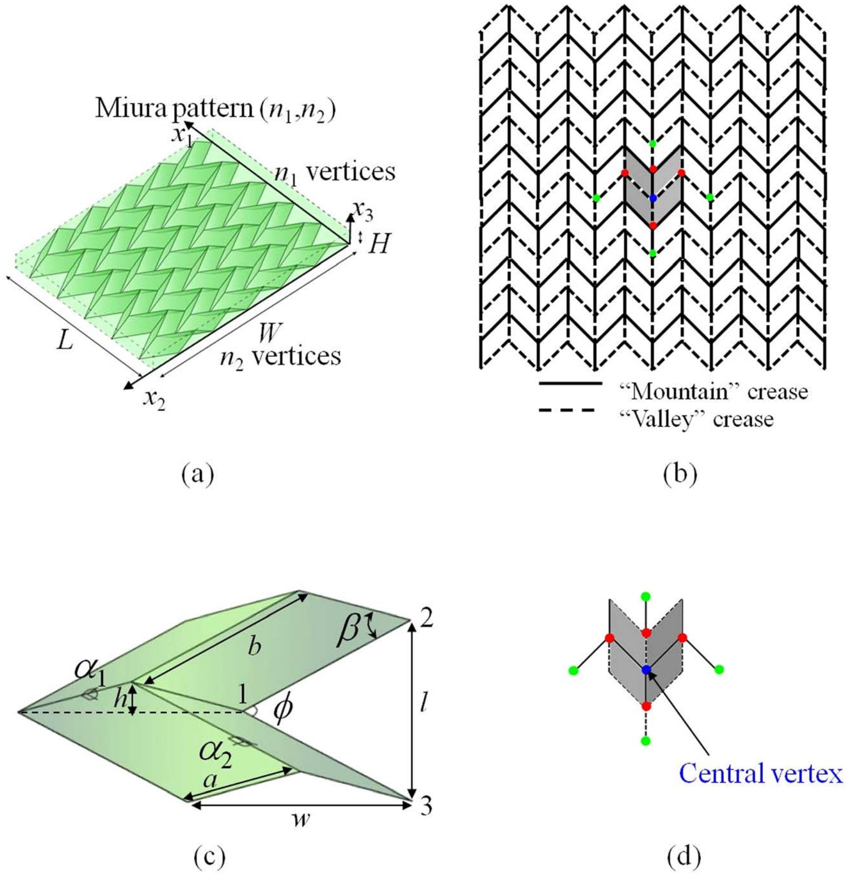

Figure 1 | Illustrations of Miura-ori. (a) A Miura-ori (n_1, n_2) in its folded state with n_1 vertices in x_1 direction, n_2 vertices in x_2 direction. x_3 is the out-of-plane direction. Specifically for this illustration, $n_1 = 11$, $n_2 = 11$, $\beta = 45°$ and $a/b = 1/\sqrt{2}$. (b) A Miura-ori in its planar state, corresponding to (a). The solid lines represent "mountain" creases that remain on the top after folding. The dashed lines represent "valley" creases that remain on the bottom after folding. (c) A unit cell of a Miura-ori. α_1,α_2 are two dihedral angles. In each parallelogram, the length of the short side is a and that of the long side is b, with the acute angle of β. The projected angle between the two ridges is ϕ. The size of the unit cell is l, w, and h, in x_1, x_2, and x_3 directions, respectively. (d) A non-local element for Miura-ori that focuses on the central vertex.

direction. Its corresponding planar state is shown in Fig. 1b. The geometry of a Miura-ori is defined by many identical rigid parallelogram faces (with four gray ones highlighted in Fig. 1b) linked by edges that can be folded into "mountain" and "valley" creases. The Miura-ori is a periodic structure and its unit cell is shown in Fig. 1c, where the four parallelograms are identical with the short sides of length a, the long sides of length b, and the acute angle $\beta \in [0°,90°]$. Since the necessary condition for rigid origami[16,17] states that there are $n - 3$ degrees of freedom, where n is the number of edges at one vertex, Miura-ori with $n = 4$ has only one degree of freedom. Therefore, if the shape of a parallelogram face is prescribed, i.e. β, a and b are given, one parameter $\phi \in [0°,2\beta]$, the projection angle between two ridges, can be used to characterize the folding of the unit cell of Miura-ori, with $\phi = 2\beta$ for the planar state and $\phi = 0°$ for the completely collapsed state. The size of the unit cell is $l = 2b\sin(\phi/2)$, $w = 2a\dfrac{\cos\beta}{\cos(\phi/2)}$, and $h = \dfrac{a\sqrt{\sin^2\beta - \sin^2(\phi/2)}}{\cos(\phi/2)}$, in x_1, x_2, and x_3 directions, respectively. It is noted that the length of the "tail" $b\cos(\phi/2)$ is not considered in the unit cell[15]. The periodicity of this pattern only requires two dihedral angles $\alpha_1 \in [0°,180°]$ and $\alpha_2 \in [0°,180°]$ to characterize the geometry (Fig. 1c), which are given by

$$\alpha_1 = \cos^{-1}\left[1 - 2\frac{\sin^2(\phi/2)}{\sin^2\beta}\right],$$
$$\alpha_2 = \cos^{-1}\left[1 - 2\cot^2\beta\tan^2(\phi/2)\right] \quad (1)$$

and equal 180° for the planar state and 0° for the completely collapsed state. When the whole structure of a Miura-ori is put in an imaginary box with the dashed lines as the boundaries (Fig. 1a), the dimension of the whole Miura-ori is then given by

$$L = (n_1 - 1)b\sin(\phi/2),$$
$$W = (n_2 - 1)a\frac{\cos\beta}{\cos(\phi/2)} + b\cos(\phi/2), \quad (2)$$
$$H = \frac{a\sqrt{\sin^2\beta - \sin^2(\phi/2)}}{\cos(\phi/2)}$$

and thus the imaginary volume occupied by this Miura-ori is given by

$$V = L \times H \times W. \quad (3)$$

Apparently even the Miura-ori is periodic, its size in x_2 direction (i.e. W) is not proportional to its counterpart for the unit cell, w, due to the existence of the "tail" with length $b\cos(\phi/2)$. Consequently, it is not accurate to use the unit cell to study the size change of a whole Miura-ori (e.g., Poisson's ratio), particularly for smaller patterns (e.g., used in[15,20]).

In-plane Poisson's ratio of Miura-ori. In-plane Poisson's ratio of Miura-ori is believed to be negative from intuitive observations and as testified by some theoretical studies using the unit cell (Fig. 1c)[15,20]. An accurate mean to define the Poisson's ratio is to use the size of a whole Miura-ori, instead of using the unit cell. Specifically, the in-plane Poisson's ratio ν_{12} is defined as $\nu_{12} = -\left.\frac{\varepsilon_{11}}{\varepsilon_{22}}\right|_{\varepsilon_{22}\to 0}$, where $\varepsilon_{11} = \frac{dL}{L}$ and $\varepsilon_{22} = \frac{dW}{W}$ are the infinitesimal strains in x_1- and x_2-directions, respectively. Using equation (2), the in-plane Poisson's ratio ν_{12} is obtained as

$$\nu_{12} = -\cot^2(\phi/2)\frac{(n_2-1)\eta\cos\beta + \cos^2(\phi/2)}{(n_2-1)\eta\cos\beta - \cos^2(\phi/2)}, \tag{4}$$

where $\eta = a/b$. Another in-plane Poisson's ratio ν_{21} is just the reciprocal of ν_{12}. Figure 2a shows the contour of ν_{12} as a function of angle ϕ and a combination parameter $(n_2 - 1)\eta\cos\beta$. Clearly, ν_{12} can be negative or positive, which is different from commonly observed negative in-plane Poisson's ratio. The boundary separating the negative and positive regimes of ν_{12} is defined by vanishing the denominator of ν_{12}, i.e., $(n_2 - 1)\eta\cos\beta = \cos^2(\phi/2)$. At this boundary, ν_{12} flips between positive and negative infinities; thus $\nu_{12} \in [-\infty, +\infty]$. For one scenario, where $n_2 = 5$ (small pattern), $\eta = 1/2$, $\beta = 78.5^\circ$, and thus $(n_2 - 1)\eta\cos\beta < 1$, ν_{12} is positive for $\phi \in [0, 101.5^\circ]$ and changes to negative for $\phi \in [101.5^\circ, 2\beta]$. For another scenario, $n_2 = 13$ (large pattern), $\eta = 1/\sqrt{2}$, $\beta = 45^\circ$, and thus $(n_2 - 1)\eta\cos\beta > 1$, ν_{12} stays negative, as reported by others using the unit cell[15,20]; and the Miura-ori becomes an auxetic material. Similar analysis can be applied on the out-of-plane Poisson's ratios. Details can be found in the Supplementary Information, Section "Out-of-plane Poisson's Ratio".

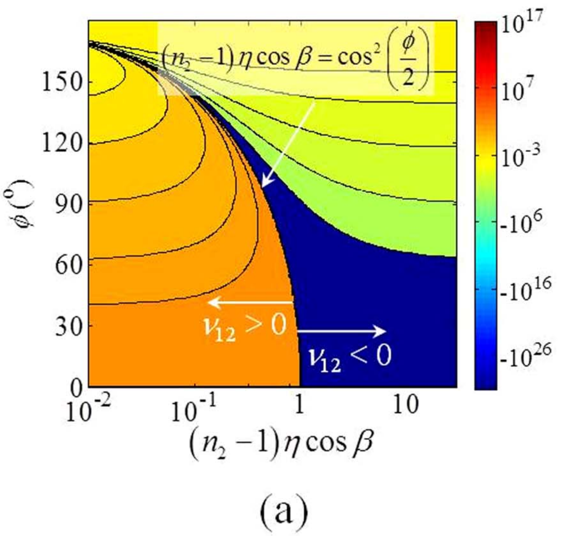

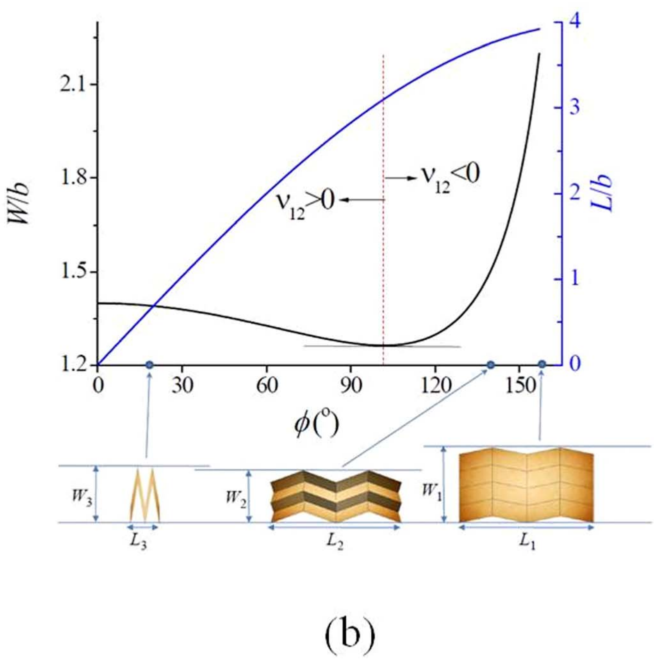

Figure 2 | Poisson's ratios of Miura-ori. (a) Contour plot of in-plane Poisson's ratio ν_{12} as a function of ϕ and the combined parameter $(n_2 - 1)\eta\cos\beta$. (b) Explanation of negative and positive in-plane Poisson's ratio ν_{12}.

Figure 2b provides an intuitive explanation of the sign change in the in-plane Poisson's ratio ν_{12}. For the specific example with $n_1 = n_2 = 5$, $\eta = 1/2$ and $\beta = 78.5^\circ$, the size of this Miura pattern in x_1 direction, L, decreases monotonically from the planar state to the collapsed state, which is pictorially shown in the three insets for $\phi = 157^\circ (=2\beta)$, $\phi = 140^\circ$, and $\phi = 20^\circ$ with $L_1 > L_2 > L_3$. In contrast to L, the respective size of this pattern in the x_2 direction, W, does not change monotonically with the angle ϕ. From the planar state to the collapsed state, $W_1 > W_2$ but $W_2 < W_3$, which gives $\nu_{12} < 0$ when L and W change in the same direction and $\nu_{12} > 0$ when L and W change in the opposite direction. The non-monotonic change of W is due to the "tail" term $b\cos(\phi/2)$ in equation (2), which was missed in previous studies[15,20]. As shown in the Supplementary Information, Section "Change of Length W" for more details, the two terms in W (equation (2)) dominate at different stage of folding.

In addition to the negative and positive in-plane Poisson's ratio of the Miura-ori, the ranges of Poisson's ratios, specifically, $\nu_{12} \in [-\infty, +\infty]$, $\nu_{13} \in [0, \infty]$, $\nu_{23} \in [-\infty, \infty]$ (see Supplementary Information, Section "Out-of-plane Poisson's Ratio") are also fascinating if the range of Poisson's ratio for common materials is considered as the reference, i.e., $\nu \in [-1, 0.5]$. Now we interpret these fascinating phenomena in terms of shear and bulk modulus of Miura-ori.

Miura-ori subjected to shear and hydrostatic deformation. To study the shear deformation that is non-uniform across the Miura-ori, we developed a numerical approach to characterize the geometric features of the Miura-ori, i.e., the non-local interactions between rigid faces. As shown in Fig. 1b, the vertex marked by the solid blue dot not only interacts with its nearest-neighboring vertices (marked by the solid red dots) through the rigid faces, but also its second-neighboring vertices (marked by the solid green dots) through dihedral angles. Thus the interactions between vertices are non-local. This non-local nature is ubiquitous in rigid origami and can be more complicated for other patterns, which can be further illustrated by the Ron Resch pattern[21], detailed in the Supplementary Information, Section "Non-local Interactions in the Ron Resch Pattern" (e.g., Supplementary Fig. S3). We developed a non-local finite element based model and Fig. 1d shows the non-local element for Miura-ori. Details can be found in Methods.

Supplementary Figure S4 shows a deformed state of a ($n_1 = 13$, $n_2 = 13$) Miura-ori subjected to a finite shear force in the negative x_1 direction. Here it is noticed that an initially periodic Miura-ori deforms non-uniformly under shear loading, which disables the definition of a shear modulus. It is seen that the Miura-ori responds in an opposite way to shear force. Specifically and clearly, the vertical lines tilt to the positive x_1 direction, as the shear force is applied along the negative x_1 direction. This opposite relationship is thus consistent with $\nu_{12} \in [-\infty, +\infty]$.

The bulk modulus K of Miura-ori can be defined the same way as that in continuum mechanics to link the hydrostatic pressure p and the volumetric strain $\theta (= \varepsilon_{11} + \varepsilon_{22} + \varepsilon_{33})$,

$$\frac{1}{K}=\frac{\theta}{p}\bigg|_{p=0}, \quad (5)$$

Using the principle of superposition (details given in the Supplementary Information, Section "Bulk Modulus of Miura-ori"), the bulk modulus K is given by

$$\frac{1}{K}=\frac{1-\nu_{21}-\nu_{31}}{E_{11}}+\frac{1-\nu_{12}-\nu_{32}}{E_{22}}+\frac{1-\nu_{13}-\nu_{23}}{E_{33}}, \quad (6)$$

where $E_{11}=\frac{d\sigma_{11}}{d\varepsilon_{11}}\Big|_{d\varepsilon_{11}=0}$, $E_{22}=\frac{d\sigma_{22}}{d\varepsilon_{22}}\Big|_{d\varepsilon_{22}=0}$, $E_{33}=\frac{d\sigma_{33}}{d\varepsilon_{33}}\Big|_{d\varepsilon_{33}=0}$ are the tangential moduli of the stress-strain curve. Using the work conjugate relation, stresses are expressed as $\sigma_{11}=\frac{\partial W_{tot}}{\partial \varepsilon_{11}}$, $\sigma_{22}=\frac{\partial W_{tot}}{\partial \varepsilon_{22}}$, $\sigma_{33}=\frac{\partial W_{tot}}{\partial \varepsilon_{33}}$, where $W_{tot}=U_{tot}/V$ is the elastic energy density with U_{tot} given by Supplementary Eq. S2 and V given by equation (3). As shown in the Supplementary Information, Section "Range of Tensile and Bulk Modulus" for details, the tensile (E_{11}, E_{22}, E_{33}) and bulk moduli (K) have a wide range of variation and some of them vary from 0 to infinity, such as K.

Ron Resch pattern and its buckling resistance. Next we study a non-periodic rigid origami folding, namely a Ron Resch pattern, using the developed non-local finite element approach. The Ron Resch pattern and its non-local elements are given in Supplementary Fig. S3. To illustrate the non-periodicity, several Ron Resch patterns (specifically, a Ron Resch dome, a tube and a stingray) have been studied and the histograms of the three dihedral angles β_1, β_2, and β_3 are shown in Supplementary Fig. S5. It is obvious that the Ron Resch pattern is non-periodic and the importance of a universal numerical platform to study this type of rigid origami is thus apparent. We first study the buckling resistance of a Ron Resch tube (Fig. 3a). A Ron Resch tube in its folded state contains many equilateral triangles. As shown in the zoom-in details in Fig. 3a, the dihedral angles $\beta_1\in[0°,90°]$ and $\beta_1\in[90°,180°]$. Because of the folded state, the centroids of these equilateral triangles form spikes pointing to the central axis of the Ron Resch tube as shown in the top view of Fig. 3a. The boundary condition for the axial compressive buckling is that one end of the tube is fixed and the other is subjected to a compressive force, which is the same as the Euler buckling. Figure 3b shows the compressive force normalized by k^{RR}/b varies as the compressive strain increases, and the insets show some characteristic snapshots at the compressive strains of 13%, 30% and 45% from left to right, respectively. Here k^{RR} is the spring constant of the hinges for dihedral angles (detailed in the Supplementary Information, Section "Work Conjugate Relation – Stress and Moduli for Miura-ori"), and b is the size of the right triangles (Supplementary Fig. S3). It is interesting to find that buckling does not occur, which can be explained by the negative Poisson's ratio. Upon compression, the two dihedral angles β_1 and β_2 decrease, which lead to the further pushing the spikes towards the central axis of the tube. Thus the compression leads to a shorter tube with smaller radius due to the negative Poisson's ratio (the leftmost inset of Fig. 3b). Further compression leads to an even smaller tube radius (the middle inset of Fig. 3b). Eventually, the equilateral triangles form completely folded states, which is captured by $\beta_1=0°$, $\beta_2=120°$ and results in a much smaller tube radius (the rightmost inset of Fig. 3b). At the completely folded state, the tube cannot be further compressed because of the rigidity. Thus, axial compressive force does not lead to the buckling of a Ron Resch tube.

Load bearing capability of a Ron Resch plate. This intriguing buckling resistance phenomenon motivates a further study of the load bearing capability of the Ron Resch pattern. The compressive load applied on top of a Ron Resch dome leads to a completely compact and flat state (namely, a Ron Resch plate), where the equilateral triangles collapse to three-fold structures with $\beta_1=0°$, $\beta_2=120°$, and $\beta_3=90°$ (Fig. 3c). Figure 3d shows the striking load bearing capability of a Ron Resch dome folded from a single sheet of 20-lb copy paper: a 32.4 lb load is carried by a Ron Resch plate with actual mass 4.54 g. This remarkable capability is mainly a result of the folded structure, not the material properties of the paper, which suggests that origami can produce exceptional mechanical metamaterials. Figure 3e shows snapshots of the bottom of Ron Resch plate when 3-lb load (left panel) and 32.4-lb load are applied (right panel). It is found that at the failure point (where the 32.4-lb load is applied), the tips of the three-fold structures are flattened and instability occurs. To compare the load bearing capability of a Ron Resch plate with three-fold supporting structures and commonly seen six-fold ones that are used in airplane wings, the buckling analysis is conducted to compute their critical compressive loads P_{cr} by using finite element package ABAQUS (details are given in the Supplementary Information, Section "Buckling Analysis of a Ron Resch Plate and a Six-Fold Supporting Structure"). Figures 3f and 3g show the first buckling modes for the Ron Resch plate and the six-fold structure. By assigning the same geometric parameters (including thickness and height of the support) and material properties (including elastic modulus and Poisson's ratio), P_{cr} of the Ron Resch plate is about 50% larger than that of the six-fold structure. Though the six-fold structure has higher symmetry to increase P_{cr} in a linear fashion (i.e., $P_{cr}\sim$ order of symmetry), the decreasing height of the support for the Ron Resch plate from the center to the surroundings increases P_{cr} in a quadratic fashion (i.e., $P_{cr}\sim 1/\text{height}^2$), which endows a higher load bearing capability of the Ron Resch plate. This result suggests that generalized Ron Resch patterns with higher order symmetry[22] would have even greater load bearing capability.

Discussion

This paper paves the ways towards the study of interesting and unique geometric and mechanical properties of origami structures as mechanical metamaterials. It is expected that through a combination of this approach and multiphysics simulations (e.g., COMOSL Multiphysics), more interesting properties can be explored. For example, the negative response between shear force and deformation, and infinite tensile and bulk modulus may lead to some unique sound and vibration behaviors. When integrated with functional materials on origami patterns with micrometer feature sizes (e.g., the size of its rigid faces), such as nanowires and two-dimensional materials, the foldability of the origami pattern would provide unique tunable metamateirals with intriguing optical, electrical and magnetic properties, which is in fact under pursue. When combined with applications, the analysis of origami as mechanical metamaterials can help to guide the development of origami based devices[8,9]. As all of these properties and applications are rooted from the way of folding, origami also provides a unique and powerful way on manufacturing. For example, plywood with unusually strong load bearing capability at the completed folded state can be manufactured in large-scale and low-cost by pre-creasing the wood panel based on the Ron Resch pattern. It is thus believed that origami may provide many interesting applications in science and engineering.

Methods

Non-local finite element method. Starting from the energy perspective, the elastic energy stored in a folded state is just the rotational energy at the creases since all the faces are rigid. If the creases are considered as elastic hinges, the elastic energy takes the quadratic term of the dihedral angels between creases. For the Miura-ori, the elastic energy can be written as

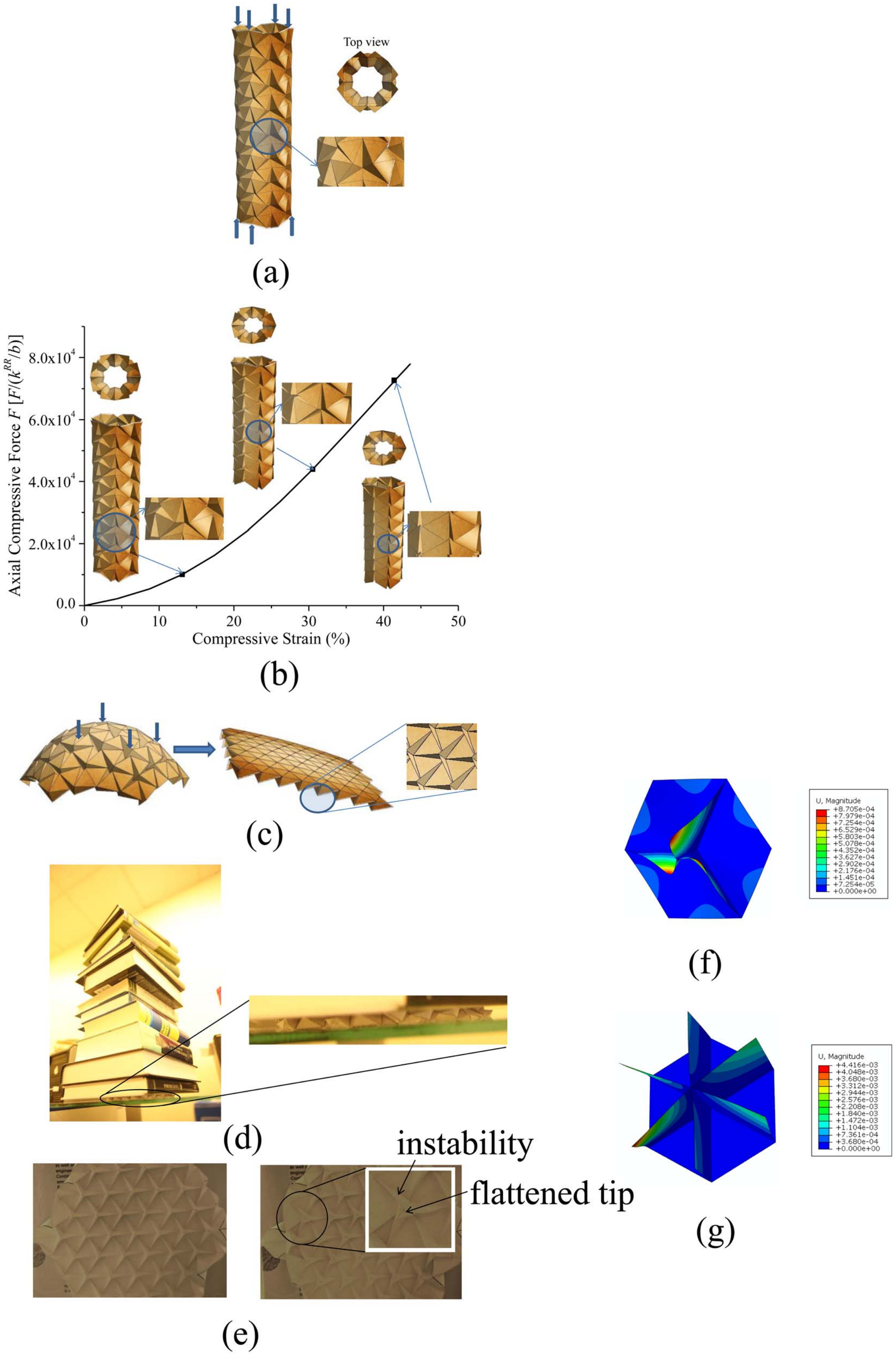

Figure 3 | Load bearing of Ron Resch patterns. (a) A Ron Resch tube subjected to an axial compressive load, where the top view is given for the cross-section before the load is applied. (b) Normalized axial compressive force as a function of axial strain. Three representative states are shown as the insets at different strain levels. Their cross-sections and zoom-ins are also shown. Same scales are used in (a) and (b). (c) Illustration of a Ron Resch dome deforms to a completely collapsed state upon compressive load from the top, where the three-fold supporting structure is shown in the inset. (d) Photographic image showing the load bearing capability of a Ron Resch pattern at its completely collapsed state. (e) Photographic images showing the three-fold structures before (left panel) and after (right panel) the failure point is reached. The inset shows the instability. (f) Finite element simulation showing the first buckling mode of a Ron Resch plate with a three-fold supporting structure. (g) Finite element simulation showing the first buckling mode of a six-fold supporting structure.

$$U_{total} = \sum_{\alpha_1} \frac{1}{2} k_1^{Mo} \left(\alpha_1 - \alpha_{1,eq}\right)^2 + \sum_{\alpha_2} \frac{1}{2} k_2^{Mo} \left(\alpha_2 - \alpha_{2,eq}\right)^2, \quad (7)$$

where k_1^{Mo} and k_2^{Mo} are the spring constants of the hinges for dihedral angles α_1 and α_2 for Miura-ori (superscript "Mo"), respectively; $\alpha_{1,eq}$ and $\alpha_{2,eq}$ are the corresponding dihedral angles for α_1 and α_2 at the undeformed state (or equivalently, just folded state); the summation runs over all dihedral angles. Similarly, the elastic energy can be readily constructed for the Ron Resch pattern,

$$U_{total} = \sum_{\beta_1} \frac{1}{2} k_1^{RR} \left(\beta_1 - \beta_{1,eq}\right)^2 + \sum_{\beta_2} \frac{1}{2} k_2^{RR} \left(\beta_2 - \beta_{2,eq}\right)^2 + \sum_{\beta_3} \frac{1}{2} k_3^{RR} \left(\beta_3 - \beta_{3,eq}\right)^2, \quad (8)$$

where the superscript "RR" denotes the Ron Resch pattern and the subscripts have a similar meaning as explained for the Miura-ori. It is reasonable to take $k_1^{Mo} = k_2^{Mo} = k^{Mo}$, and $k_1^{RR} = k_2^{RR} = k_3^{RR} = k^{RR}$, for paper folding (although in most machine-made papers, the fibers tend to run in one direction and so the hinge constants for edges running in different directions will be different).

Because the dihedral angles are completely determined by the coordinates of vertices in rigid origami, the elastic energy can also be expressed as a function of coordinates of vertices, i.e., $U_{total} = U_{total}(\mathbf{x})$, where $\mathbf{x} = (\mathbf{x}_1, \mathbf{x}_2, \cdots, \mathbf{x}_N)^T$ and $\mathbf{x}_i$ is the position of a vertex i, and N is the total number of the vertices. When the external load $\bar{\mathbf{F}}_i$ is applied at vertex i, the total potential energy is $\Pi_{total}(\mathbf{x}) = U_{total} - \sum_i \bar{\mathbf{F}}_i \cdot \mathbf{x}_i$. The equilibrium state of a rigid origami corresponds to a state of minimum energy and can be given by

$$\frac{\partial \Pi_{total}}{\partial \mathbf{x}} = 0, \quad (9)$$

which needs to be solved to reach the equilibrium state of a rigid origami. There are many approaches that can be utilized to solve Supplementary Eq. S3, such as the conjugate gradient method and steepest descent method that just use the first derivatives of Π_{total}, or the finite element method that uses both the first derivative (as the non-equilibrium force $\mathbf{P} = -\frac{\partial \Pi_{total}}{\partial \mathbf{x}}$) and the second derivatives (as the stiffness matrix $\mathbf{K} = \frac{\partial^2 \Pi_{total}}{\partial \mathbf{x} \partial \mathbf{x}}$) of Π_{total}. The governing equation for the finite element method is

$$\mathbf{K} \cdot \mathbf{u} = \mathbf{P}, \quad (10)$$

where $\mathbf{u} = \mathbf{x} - \mathbf{x}^{(0)}$ is the displacement of the vertices with $\mathbf{x}^{(0)}$ as the initial position of the vertices. For nonlinear systems, equation (10) is solved iteratively until the equilibrium characterized by the vanishing non-equilibrium force $\mathbf{P} = \mathbf{0}$. For discrete vertices in rigid origami that has a great deal of similarity with atomic systems, the finite element method has been extended to capture the non-local interactions[23,24].

There are two aspects to consider when the finite element method is used. Firstly, to calculate the non-equilibrium force $\mathbf{P}$ and stiffness matrix $\mathbf{K}$, the elastic energy U_{total} needs to be explicitly written as a function of vertex coordinates, which is detailed in the Supplementary Information, Section "Nonlinearity of the Elastic Energy with respect to the Coordinates of Vertices". Therefore, iteration is needed. Secondly, non-local elements are required to capture the non-local interactions within a single element. For example, those nine vertices marked by blue, red and green dots in Fig. 1d form one non-local element for the Miura-ori, focusing on the central vertex marked by the blue dot. Similar non-local elements (i.e., all solid circles and open circles in Supplementary Fig. S3) are constructed for the Ron Resch pattern, as shown in Supplementary Fig. S3. It may be noticed that the definition of non-local elements depends on specific rigid origami patterns and in each pattern different elements are formed for different types of vertices. These non-local elements are implemented in the commercial finite element package, ABAQUS, via its user defined elements (UEL).

1. Bertoldi, K., Reis, P. M., Willshaw, S. & Mullin, T. Negative Poisson's ratio behavior induced by an elastic instability. *Adv. Mater.* **22**, 361–366 (2010).
2. Kadic, M., Buckmann, T., Stenger, N., Thiel, M. & Wegener, M. On the practicability of pentamode mechanical metamaterials. *Appl. Phys. Lett.* **100**, 191901 (2012).
3. Lee, J. *et al.* A mechanical metamaterial made from a DNA hydrogel. *Nat. Nanotechnol.* **7**, 816–820 (2012).
4. Zheng, X. *et al.* Ultralight, ultrastiff mechanical metamaterials. *Science* **344**, 1373–1377 (2014).
5. Gardner, J. P. *et al.* The James Webb space telescope. *Space Sci. Rev.* **123**, 485–606 (2006).
6. Cromvik, C. & Eriksson, K. *Airbag folding based on origami mathematics* (Chalmers University of Technology, Göteborg, 2006).
7. Kuribayashi, K. *et al.* Self-deployable origami stent grafts as a biomedical application of Ni-rich TiNi shape memory alloy foil. *Mater. Sci. Eng. A-Struct. Mater. Prop. Microstruct. Process.* **419**, 131–137 (2006).
8. Tang, R. *et al.* Origami-enabled deformable silicon solar cells. *Appl. Phys. Lett.* **104**, 083501 (2014).
9. Song, Z. *et al.* Origami lithium-ion batteries. *Nat. Commun.* **5**, 3140; doi: 10.1038/ncomms4140 (2014).
10. Lang, R. J. *Origami design secrets*, 2nd edn (CRC Press, Boca Raton, 2011).
11. Lang, R. J. A computational algorithm for origami design. In: *Proc. 12th Annual ACM Symp. on Computational Geometry* 98–105 (1996).
12. Cerda, E. & Mahadevan, L. Confined developable elastic surfaces: cylinders, cones and the Elastica. *Proc R Soc A-Math. Phys. Eng. Sci.* **461**, 671–700 (2005).
13. Dias, M. A. & Santangelo, C. D. The shape and mechanics of curved fold origami structures. *Europhys. Lett.* **100**, 54005 (2012).
14. Dias, M. A., Dudte, L. H., Mahadevan, L. & Santangelo, C. D. Geometric mechanics of curved crease origami. *Phys. Rev. Lett.* **109**, 114301 (2012).
15. Wei, Z. Y., Guo, Z. V., Dudte, L., Liang, H. Y. & Mahadevan, L. Geometric mechanics of periodic pleated origami. *Phys. Rev. Lett.* **110**, 215501 (2013).
16. Belcastro, S.-M. & Hull, T. C. Modeling the folding of paper into three dimensions using affine transformations. *Linear Algebra Appl.* **348**, 273–282 (2002).
17. Belcastro, S.-M. & Hull, T. C. *Origami 3* (A K Peters/CRC Press, Natick, 2002).
18. Tachi, T. Simulation of rigid origami. In: *Origami 4, Proceedings of 4OSME: 4th International Conference on Origami Science, Mathematics and Education* (ed(eds Lang, R. J.) (2009).
19. Miura, K. *Method of packaging and deployment of large membranes in space* (Institute of Space and Astronomical Sciences, Tokyo, 1985).
20. Schenk, M. & Guest, S. D. Geometry of Miura-folded metamaterials. *Proc. Natl. Acad. Sci. U S A* **110**, 3276–3281 (2013).
21. Resch, R. D., inventor & Resch, R. D., assignee. Self-supporting structural unit having a series of repetitious geometrical modules. United States patent US 3,407,558. 1968 Oct 29.
22. Tachi, T. Designing freeform origami tessellations by generalizing Resch's patterns. *J. Mech. Design* **135**, 111006 (2013).
23. Liu, B., Huang, Y., Jiang, H., Qu, S. & Hwang, K. C. The atomic-scale finite element method. *Comput. Meth. Appl. Mech. Eng.* **193**, 1849–1864 (2004).
24. Liu, B., Jiang, H., Huang, Y., Qu, S., Yu, M. F. & Hwang, K. C. Atomic-scale finite element method in multiscale computation with applications to carbon nanotubes. *Phys. Rev. B* **72**, 035435 (2005).

Acknowledgments

We acknowledge the seed grant support from the Office of Associate Dean for Research at Ira A. Fulton School of Engineering, and Office of Knowledge Enterprise and Development, Arizona State University.

Author contributions

C.L., D.K. and H.J. carried out and designed experiments and analysis. C.L., D.K. and H.J. wrote the paper. C.L., D.K., G.K., H.Y. and H.J. commented on the paper.

Additional information

Supplementary information accompanies this paper at http://www.nature.com/scientificreports

Competing financial interests: The authors declare no competing financial interests.

How to cite this article: Lv, C., Krishnaraju, D., Konjevod, G., Yu, H. & Jiang, H. Origami based Mechanical Metamaterials. *Sci. Rep.* **4**, 5979; DOI:10.1038/srep05979 (2014).

Supplementary Information

for

Origami based Mechanical Metamaterials

By *Cheng Lv, Deepakshyam Krishnaraju, Goran Konjevod, Hongyu Yu, and Hanqing Jiang**

[*] Prof. H. Jiang, C. Lv, D. Krishnaraju, Dr. G. Konjevod

School for Engineering of Matter, Transport and Energy

Arizona State University, Tempe, AZ 85287 (USA)

E-mail: hanqing.jiang@asu.edu

[*] Prof. H. Yu

School of Earth and Space Exploration

School of Electrical, Computer and Energy Engineering

Arizona State University, Tempe, AZ 85287 (USA)

Change of Length W

The length W is given by Eq. (2) of the main text. Figure 1Sa shows the derivatives of W's two terms, i.e., $\frac{\partial}{\partial\phi}\left[(n_2-1)\eta\frac{\cos\beta}{\cos(\phi/2)}\right]$ and $-\frac{\partial\left[\cos(\phi/2)\right]}{\partial\phi}$, along with W, as a function of ϕ, for $n_1=n_2=5$, $\eta=1/2$ and $\beta=78.5^\circ$, the same parameters used in Fig. 2b. It can be seem that these two derivatives work against each other with $\frac{\partial}{\partial\phi}\left[(n_2-1)\eta\frac{\cos\beta}{\cos(\phi/2)}\right]>0$ to decrease W, while with $\frac{\partial\left[\cos(\phi/2)\right]}{\partial\phi}<0$ to increase W, from a planar state to a collapsed state. Therefore, the one among these two derivatives with larger absolute value dominates the change of W. It is apparent that when one folds a Miura-ori from its planar state to a collapsed state, $\frac{\partial}{\partial\phi}\left[(n_2-1)\eta\frac{\cos\beta}{\cos(\phi/2)}\right]>0$ dominates firstly to decrease W. Once the stationary point is reached, $\frac{\partial\left[\cos(\phi/2)\right]}{\partial\phi}<0$ starts to dominate and increase W.

Out-of-plane Poisson's Ratio

Using Eq. (2) in the main text, the out-of-plane Poisson's ratios, related to in-plane strains upon height change, are given by

$$
\begin{aligned}
\nu_{13} &= -\left.\frac{\varepsilon_{11}}{\varepsilon_{33}}\right|_{\varepsilon_{33}\to 0} = \frac{\cot^2(\phi/2)\left[\sin^2\beta-\sin^2(\phi/2)\right]}{\cos^2\beta} \\
\nu_{23} &= -\left.\frac{\varepsilon_{22}}{\varepsilon_{33}}\right|_{\varepsilon_{33}\to 0} = \frac{\left[\sin^2\beta-\sin^2(\phi/2)\right]\left[(n_2-1)\eta\cos\beta-\cos^2(\phi/2)\right]}{\cos^2\beta\left[(n_2-1)\eta\cos\beta+\cos^2(\phi/2)\right]}
\end{aligned}
\tag{S1}
$$

where $\varepsilon_{33}=\frac{dH}{H}$ is the strain in x_3-direction. Figure S1b shows that ν_{13} is positive across the entire range of ϕ, due to $\phi\in\left[0^\circ,2\beta\right]$, and monotonically decreases from ∞ to 0 as the Miura-ori varies from its completely collapsed state ($\phi = 0^\circ$) to the planar state ($\phi = 2\beta$), i.e., $\nu_{13} \in [0,\infty]$. For an extreme case when $\beta \to 90^\circ$ or $\phi \to 0^\circ$, $\nu_{13} \to \infty$. Figure S1c shows ν_{23} for $n_2 = 13$ and $\eta = 0.5$. It is observed that ν_{23} can be both negative and positive, separated by a boundary defined by $(n_2 - 1)\eta\cos\beta = \cos^2(\phi/2)$ which is shown as the white dashed line. Figure S1c also shows that $\nu_{23} \in [-\infty,\infty]$.

Nonlinearity of the Elastic Energy with respect to the Coordinates of Vertices

Depending on the type of rigid origami and the number of dihedral angles per unit cell, the elastic energy can be always expressed by

$$U_{total} = \sum_{i=1}^{T_n} \sum_{\alpha_i} \frac{1}{2} k_i \left(\alpha_i - \alpha_{i,eq}\right)^2, \quad \text{(S2)}$$

where k_i are the stiffness constants of the dihedral angles α_i with $\alpha_{i,eq}$ as the equilibrium angle, and T_n is the number of types of dihedral angles. To obtain the stiffness matrix **K** and non-equilibrium force **P**, we need to express U_{total} in terms of the coordinates of vertices.

Considering the case of Miura-ori where T_n=2, the two dihedral angles are given as

$$\begin{aligned} \alpha_1 &= \cos^{-1}\left[1 - 2\frac{\sin^2(\phi/2)}{\sin^2\beta}\right] \\ \alpha_2 &= \cos^{-1}\left[1 - 2\cot^2\beta\tan^2(\phi/2)\right] \end{aligned}, \quad \text{(S3)}$$

where ϕ is the projection angle between two ridges. $\beta \in [0^\circ, 90^\circ]$ and $\phi \in [0^\circ, 2\beta]$. Using the distances between the three vertices 1, 2, 3 (Fig. 1c) that form this angle, ϕ can be determined by using the cosine rule,

$$\phi = \cos^{-1}\left(\frac{R_{12}^2 + R_{13}^2 - R_{23}^2}{2R_{12}R_{13}}\right), \quad \text{(S4)}$$

where R_{ij} is the distance between vertices *i* and *j*.

By combining Eqs. (S2) to (S4), a relationship between the elastic energy and the coordinates of vertices can be obtained. Clearly, this relationship is nonlinear, i.e., U_{total} is nonlinear with respect to the coordinates of vertices.

Bulk Modulus of Miura-ori

The bulk modulus *K* of Miura-ori can be defined by

$$\frac{1}{K} = \left.\frac{\theta}{p}\right|_{p=0}, \tag{S5}$$

where *p* is the hydrostatic pressure. Using the principle of superposition, when only $p\left(=\sigma_{11}\right)$ is applied and $\sigma_{22} = \sigma_{33} = 0$, we have $\theta = \left(1-\nu_{21}-\nu_{31}\right)\varepsilon_{11}$, where σ_{11}, σ_{22} σ_{33} are normal stresses in x_1, x_2, and x_3 directions, respectively. Using a similar approach for σ_{22} and σ_{33}, the bulk modulus *K* is given by $\frac{1}{K} = \left(1-\nu_{21}-\nu_{31}\right)\frac{\varepsilon_{11}}{\sigma_{11}} + \left(1-\nu_{12}-\nu_{32}\right)\frac{\varepsilon_{22}}{\sigma_{22}} + \left(1-\nu_{13}-\nu_{23}\right)\frac{\varepsilon_{33}}{\sigma_{33}}$, where $\sigma_{11} = \sigma_{22} = \sigma_{33} = p$.

For vanishing nominal stress $\sigma_{11} = \sigma_{22} = \sigma_{33} \to 0$, the tensile moduli are given by

$$\frac{1}{E_{11}} = \left.\frac{\varepsilon_{11}}{\sigma_{11}}\right|_{\sigma_{11}=0}, \quad \frac{1}{E_{22}} = \left.\frac{\varepsilon_{22}}{\sigma_{22}}\right|_{\sigma_{22}=0}, \quad \frac{1}{E_{33}} = \left.\frac{\varepsilon_{33}}{\sigma_{33}}\right|_{\sigma_{33}=0}. \tag{S6}$$

Thus the bulk modulus *K* is given by

$$\frac{1}{K} = \frac{1-\nu_{21}-\nu_{31}}{E_{11}} + \frac{1-\nu_{12}-\nu_{32}}{E_{22}} + \frac{1-\nu_{13}-\nu_{23}}{E_{33}}. \tag{S7}$$

Here the tensile moduli are the tangential moduli of the stress-strain curve, i.e., $E_{11} = \left.\frac{d\sigma_{11}}{d\varepsilon_{11}}\right|_{d\varepsilon_{11}=0}$, $E_{22} = \left.\frac{d\sigma_{22}}{d\varepsilon_{22}}\right|_{d\varepsilon_{22}=0}$, $E_{33} = \left.\frac{d\sigma_{33}}{d\varepsilon_{33}}\right|_{d\varepsilon_{33}=0}$.

Work Conjugate Relation – Stress and Moduli for Miura-ori

The elastic energy density W_{tot} for a (n_1, n_2) Miura-ori is given by

$$W_{tot} = \frac{(n_1-2)(n_2-1)\frac{1}{2}k_1^{Mo}\left(\alpha_1-\alpha_{1,eq}\right)^2 + (n_1-1)(n_2-2)\frac{1}{2}k_2^{Mo}\left(\alpha_2-\alpha_{2,eq}\right)^2}{V}, \tag{S8}$$

where

$$V = (n_1-1)ab\frac{\sin(\phi/2)}{\cos^2(\phi/2)}\left[(n_2-1)a\cos\beta + b\cos^2(\phi/2)\right]\sqrt{\sin^2\beta-\sin^2(\phi/2)} \tag{S9}$$

is the volume of this (n_1, n_2) Miura-ori. The work conjugate relation provides stress by taking derivatives of W_{tot} with respect to strains, i.e.,

$$\sigma_{11} = \frac{\partial W_{tot}}{\partial\varepsilon_{11}}, \sigma_{22} = \frac{\partial W_{tot}}{\partial\varepsilon_{22}}, \sigma_{33} = \frac{\partial W_{tot}}{\partial\varepsilon_{33}}. \tag{S10}$$

Since the Miura-ori is a periodic structure and for a given Miura-ori (i.e., fixed (n_1, n_2), a, b, and β), the deformation can be solely determined by a single parameter ϕ, these derivatives can be implemented by taking derivatives with respect to ϕ, i.e.,

$$\sigma_{11} = \frac{\partial W_{tot}/\partial\phi}{\partial\varepsilon_{11}/\partial\phi}, \sigma_{22} = \frac{\partial W_{tot}/\partial\phi}{\partial\varepsilon_{22}/\partial\phi}, \sigma_{33} = \frac{\partial W_{tot}/\partial\phi}{\partial\varepsilon_{33}/\partial\phi}. \tag{S11}$$

The strains are explicitly given by

$$\begin{aligned}
\varepsilon_{11} &= \frac{dL}{L} = 1/2\cot(\phi/2)\,d\phi \\
\varepsilon_{22} &= \frac{dW}{W} = \frac{\tan(\phi/2)}{2}\left[\frac{(n_2-1)a\cos\beta - b\cos^2(\phi/2)}{(n_2-1)a\cos\beta + b\cos^2(\phi/2)}\right]d\phi\,. \\
\varepsilon_{33} &= \frac{dH}{H} = -\frac{\tan(\phi/2)\cos^2(\beta)}{2\left[\sin^2(\beta)-\sin^2(\phi/2)\right]}d\phi
\end{aligned} \tag{S12}$$

Thus the stresses are obtained as

$$
\begin{aligned}
\sigma_{11} &= \frac{2\tan(\phi/2)}{V}\kappa \\
\sigma_{22} &= \frac{2\cot(\phi/2)}{V}\frac{(n_2-1)a\cos\beta + b\cos^2(\phi/2)}{(n_2-1)a\cos\beta - b\cos^2(\phi/2)}\kappa\,, \\
\sigma_{33} &= -\frac{2\cot(\phi/2)\left[\sin^2\beta - \sin^2(\phi/2)\right]}{\cos^2\beta}\kappa
\end{aligned}
\tag{S13}
$$

where

$$
\begin{aligned}
\kappa &= (n_1-2)(n_2-1)k_1^{Mo}\left(\alpha_1 - \alpha_{1,eq}\right)\frac{\cos(\phi/2)}{\sqrt{\sin^2\beta - \sin^2(\phi/2)}} \\
&\quad + (n_1-1)(n_2-2)k_2^{Mo}\left(\alpha_2 - \alpha_{2,eq}\right)\sqrt{\frac{\cos\beta}{\cos(\phi/2)\sqrt{\sin^2\beta - \sin^2(\phi/2)}}} - W_{tot}\frac{dV}{d\phi}
\end{aligned}
.
\tag{S14}
$$

The moduli are given by

$$
\begin{aligned}
E_{11} &= \left.\frac{d\sigma_{11}}{d\varepsilon_{11}}\right|_{\varepsilon_{11}=0} = \left.\frac{d\sigma_{11}/d\phi}{d\varepsilon_{11}/d\phi}\right|_{d\phi=0} \\
E_{22} &= \left.\frac{d\sigma_{22}}{d\varepsilon_{22}}\right|_{\varepsilon_{22}=0} = \left.\frac{d\sigma_{22}/d\phi}{d\varepsilon_{22}/d\phi}\right|_{d\phi=0}\,. \\
E_{33} &= \left.\frac{d\sigma_{33}}{d\varepsilon_{33}}\right|_{\varepsilon_{33}=0} = \left.\frac{d\sigma_{33}/d\phi}{d\varepsilon_{33}/d\phi}\right|_{d\phi=0}
\end{aligned}
\tag{S15}
$$

Implementation of Eq. (S15) leads to

$$
\begin{aligned}
E_{11} &= \frac{k^{Mo}}{ab^2}\frac{\zeta}{\xi}\tan^2(\phi/2) \\
E_{22} &= \frac{k^{Mo}}{ab^2}\frac{\zeta}{\xi}\cot^2(\phi/2)\left[\frac{(n_2-1)\eta\cos\beta + \cos^2(\phi/2)}{(n_2-1)\eta\cos\beta - \cos^2(\phi/2)}\right]^2 \\
E_{33} &= \frac{k^{Mo}}{ab^2}\frac{\zeta}{\xi}\frac{\cot^2(\phi/2)\left[\sin^2\beta - \sin^2(\phi/2)\right]^2}{\cos^4\beta}
\end{aligned}
\tag{S16}
$$

where $\zeta = 4\left[(n_1-2)(n_2-1)\cos^4(\phi/2) + (n_1-1)(n_2-2)\cos^2\beta\right]$ and $\xi = (n_1-1)\sin(\phi/2)\left[(n_2-1)\eta\cos\beta + \cos^2(\phi/2)\right]\left[\sin^2\beta - \sin^2(\phi/2)\right]^{3/2}$. Here k^{Mo} is the spring constant of the hinges for dihedral angles for Miura-ori.

Range of Tensile and Bulk Modulus

Given that $n_1 \in [3,\infty]$, $n_2 \in [3,\infty]$, and $\phi \in [0^\circ, 2\beta]$, $E_{11} \in [0,\infty]$ with 0 for the completely collapsed state ($\phi = 0^\circ$) and ∞ for the planar state ($\phi = 2\beta$), $E_{33} \in [0,\infty]$ with 0 for the planar state ($\phi = 2\beta$) and ∞ for the completely collapsed state ($\phi = 0^\circ$). E_{22} varies from a finite positive value (depending on n_1, n_2, and ϕ) to ∞ at both the planar and completely collapsed states. Figures S2a-c show the tensile moduli E_{11}, E_{22}, and E_{33} normalized by k^{Mo}/ab^2 as a function of ϕ for a few representative n_1 and n_2, and $\eta = 1/\sqrt{2}$, $\beta = 45^\circ$. Above discussed trends are observed.

Now we study the bulk modulus using Eq. (S7). Since some extreme values (e.g., 0, ∞, and $-\infty$) present in either tensile moduli or Poisson's ratios, it is interesting to study the extreme values of K. At $\phi \to 0$, $\frac{1-\nu_{21}-\nu_{31}}{E_{11}} \to \infty$, $\frac{1-\nu_{12}-\nu_{32}}{E_{22}} \to 0$, and $\frac{1-\nu_{13}-\nu_{23}}{E_{33}} \to 0$, thus the bulk modulus $K \to 0$. At $\phi \to 2\beta$, $\frac{1-\nu_{21}-\nu_{31}}{E_{11}} \to 0$, $\frac{1-\nu_{12}-\nu_{32}}{E_{22}} \to 0$, and $\frac{1-\nu_{13}-\nu_{23}}{E_{33}} \to \infty$, thus the bulk modulus $K \to 0$. Another interesting point is at a particular state (ϕ) for the prescribed n_1, n_2 and β, the right hand of Eq. (S7) vanishes, which provides an infinity bulk modulus. The vanishing of the right hand of Eq. (S7) is determined by the numerators, specifically $1-\nu_{21}-\nu_{31}$, $1-\nu_{12}-\nu_{32}$, and $1-\nu_{13}-\nu_{23}$, and again the condition of vanishing these three terms is given by their numerators. Based on Eq. (4) in the main text and Eq. (S1), the numerators of $1-\nu_{21}-\nu_{31}$, $1-\nu_{12}-\nu_{32}$, and $1-\nu_{13}-\nu_{23}$ happen to be identical,

$$\begin{aligned} &2\cos^6(\phi/2) - \cos^4(\phi/2)\left(1+\cos^2\beta\right) \\ &+(n_2-1)\eta\cos^2(\phi/2)\left(\cos\beta+\cos^3\beta\right) - 2(n_2-1)\eta\cos^3\beta \end{aligned} . \tag{S17}$$

The vanishing of the expression (S17) provides a particular state of folding characterized by the angle ϕ and dependent on n_2 to reach an infinity bulk modulus. Figure S2d shows the bulk modulus K

normalized by k^{Mo}/ab^2 as a function of ϕ for a few representative n_1 and n_2, and $\eta = 1/\sqrt{2}$, $\beta = 45^\circ$, where the signature of changing from 0 to ∞ and then 0 is represented.

Non-local Interactions in the Ron Resch Pattern

Figure S3a shows the planar state of a Ron Resch pattern, which features some equilateral triangles connected by some right triangles. The insets of Fig. S3a show two different folded states of Ron Resch patterns with the upper left one for a dome shape and the upper right one for a completely collapsed state or namely, a Ron Resch plate. Three dihedral angles, β_1, β_2, and β_3 are required to describe this rigid origami folding (Fig. S3b). When $\beta_1 = \beta_2 = \beta_3 = 180^\circ$, i.e., all triangles are in the same plane, it represents a planar state (e.g., Fig. S3a). When $\beta_1 \in \left[0^\circ, 180^\circ\right]$, $\beta_2 \in \left[0^\circ, 180^\circ\right]$, and $\beta_3 \in \left[0^\circ, 180^\circ\right]$, it corresponds to a curved state, illustrated by the upper left inset of Fig. S3a as an example. When $\beta_1 = 0^\circ$, $\beta_2 = 120^\circ$, $\beta_3 = 90^\circ$, it describes another planar but more compact state (illustrated by the upper right inset of Fig. S3a), by the name of a Ron Resch plate. It is noticed that there are two types of vertices in a Ron Resch pattern, specifically, the centroids of the equilateral triangles (e.g., the vertex marked by a solid blue dot in Fig. S3a) and vertices between the right and equilateral triangles (e.g., the vertex marked by an open blue dot in Fig. S3a). The non-local feature can be similarly observed from these two vertices. For example for the solid blue vertex, it is seen that its motion influences its nearest-neighbor vertices (i.e., the ones marked by solid red dots) through dihedral angles β_1 and β_2, and its second-neighbor vertices (i.e., the ones marked by solid green dots) through dihedral angles β_3.

Buckling Analysis of a Ron Resch Plate and a Six-Fold Supporting Structure

These two structures are all periodic so that only the unit cells are utilized to conduct the buckling analysis. Figure S6 shows the unit cell of these two structures. Same thickness, height of supporting, elastic modulus and Poisson’s ratio are assigned to the two models. The finite element package

ABAQUS is used, where the eigenvalues of the different modes can be calculated by using the built-in buckling module. Critical load then can be obtained by using

$$P_{cr}^{i^{th}} = P\lambda^{i^{th}} \tag{S18}$$

where $P_{cr}^{i^{th}}$ is the critical load for the i^{th} mode, P is the infinitesimal load applied in the simulation, $\lambda^{i^{th}}$ is the i^{th} eigenvalue. For the Ron Resch plate, 284,258 R3 (3-node triangular shell) elements are used, with the fixed displacement boundary conditions along the in-plane directions of the plate and the spike. Contact at the spike between the ground plane and the Ron Resch plate is considered. A very small concentrated load is applied at the centroid of the plate. For the six-fold supporting structure, 249,268 S4 (4-node doubly curved shell) elements are used. Same boundary conditions and loads are applied. The cross-sectional properties and material properties of these two structures are the same. Here only the first buckling mode is concerned. The buckling analysis shows that the critical load for the Ron Resch plate is 57% higher than that for the six-fold supporting structure.

Figures

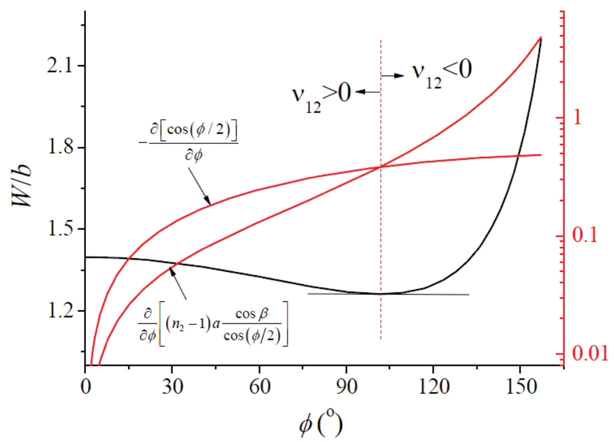

(a)

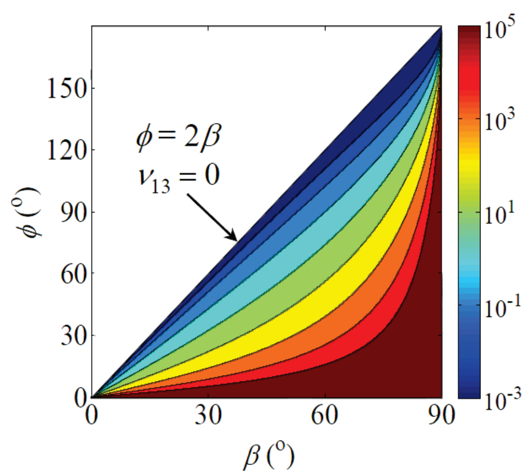

(b)

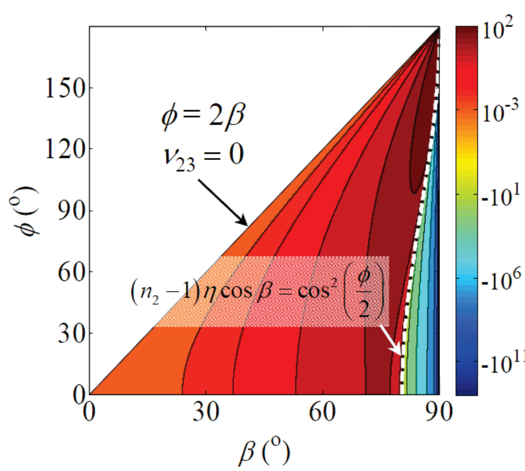

(c)

Supplementary Figure S1. Geometry characteristics of Miura-ori. (a) Change of size W. Here the change rate of W's two terms with respective to ϕ is also shown. **(b)** Contour plot of out-of-plane Poisson's ratio ν_{13} as a function of ϕ and β. **(c)** Contour plot of out-of-plane Poisson's ratio ν_{23} as a function of ϕ and β.

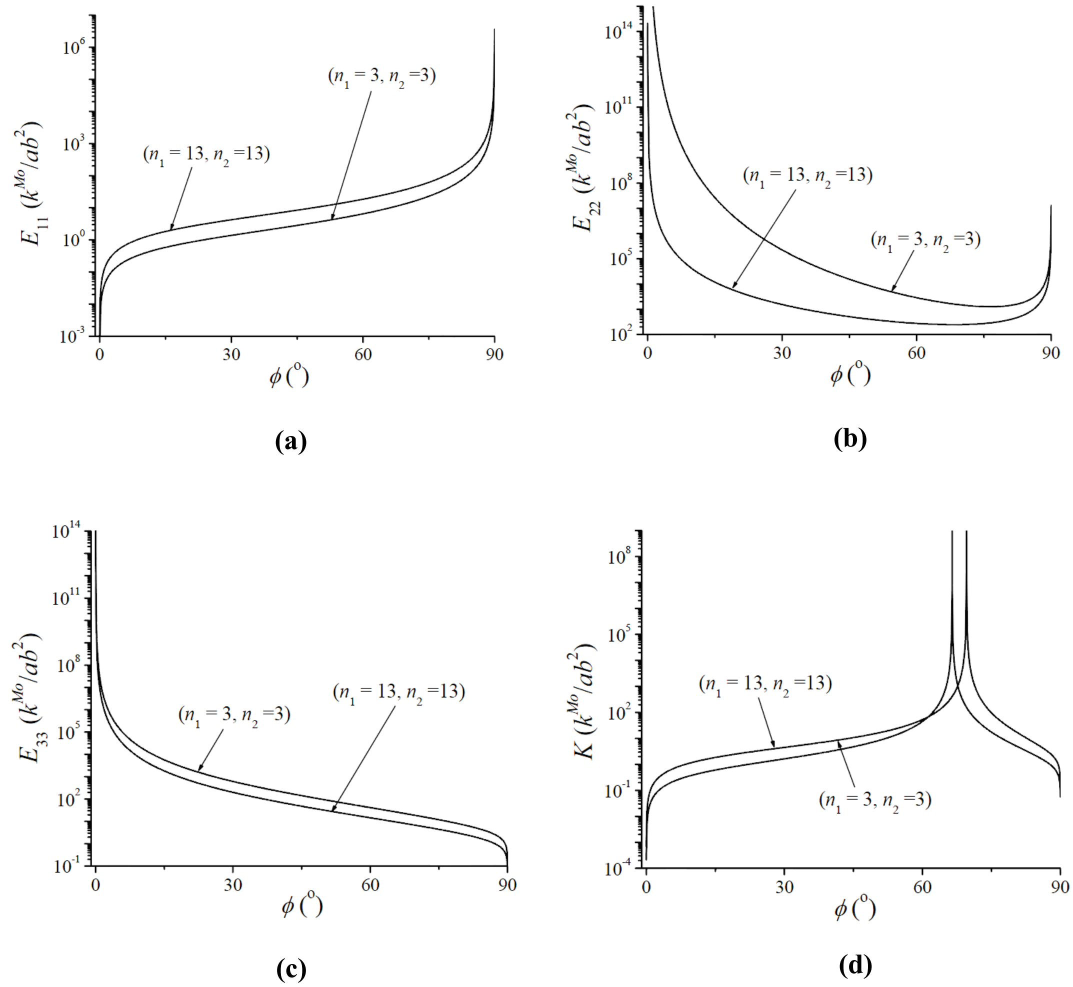

Supplementary Figure S2. Tensile and bulk moduli for the Miura-ori. **(a)** Tensile modulus E_{11} as a function of ϕ for (3,3) and (13,13) Miura-ori. **(b)** Tensile modulus E_{22} as a function of ϕ for (3,3) and (13,13) Miura-ori. **(c)** Tensile modulus E_{33} as a function of ϕ for (3,3) and (13,13) Miura-ori. **(d)** Bulk modulus K as a function of ϕ for (3,3) and (13,13) Miura-oris. Here $\eta = 1/\sqrt{2}$, $\beta = 45^{\circ}$ and all moduli are normalized by k^{Mo}/ab^2.

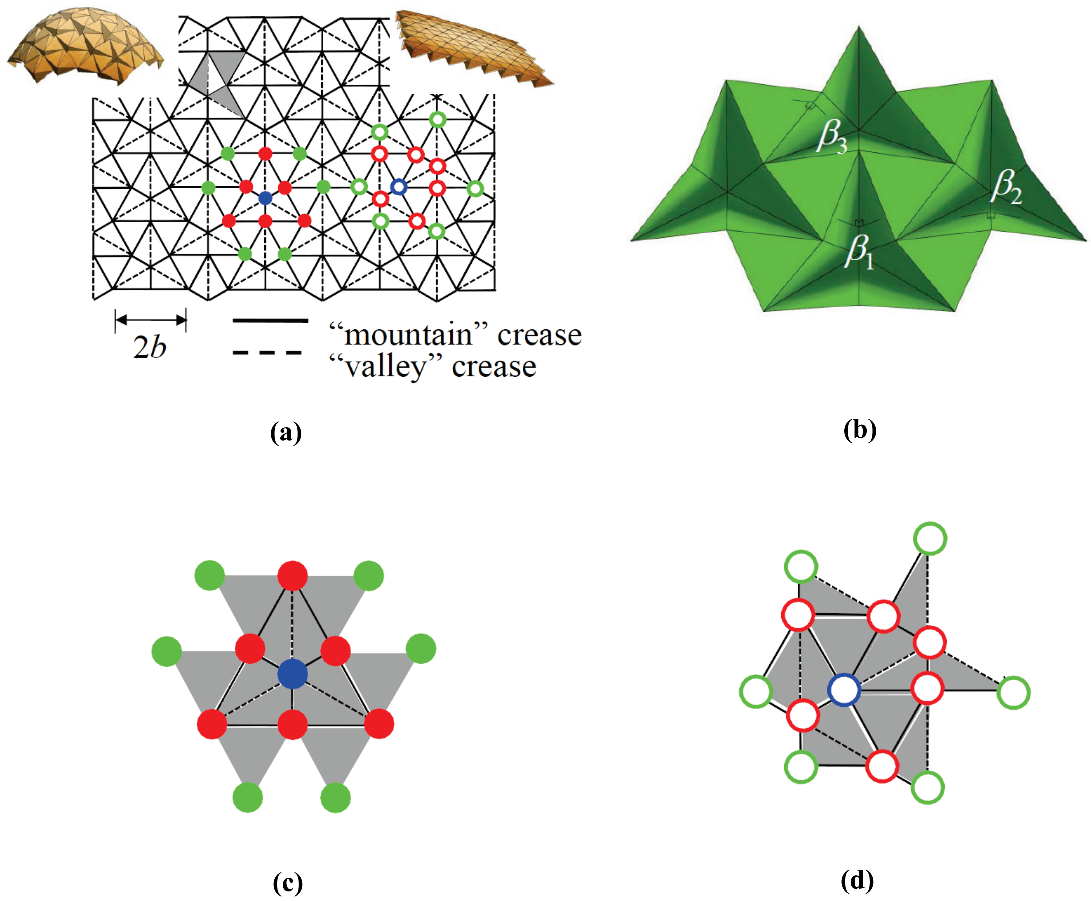

Supplementary Figure S3. Ron Resch pattern. **(a)** The planar state of a Ron Resch pattern, where the solid lines are for “mountain” creases and the dashed lines are for “valley” creases. Insets are two different folded states. On the upper left is a dome shape and the upper right is a completely collapsed state. **(b)** Three dihedral angles β_1, β_2, and β_3 are needed to describe a Ron Resch pattern. **(c)** One type of non-local element for the Ron Resch pattern with the centroid of the equilateral triangle as the central vertex. **(d)** Another type of non-local element for the Ron Resch pattern with the intersections between pleated triangles as the central vertex.

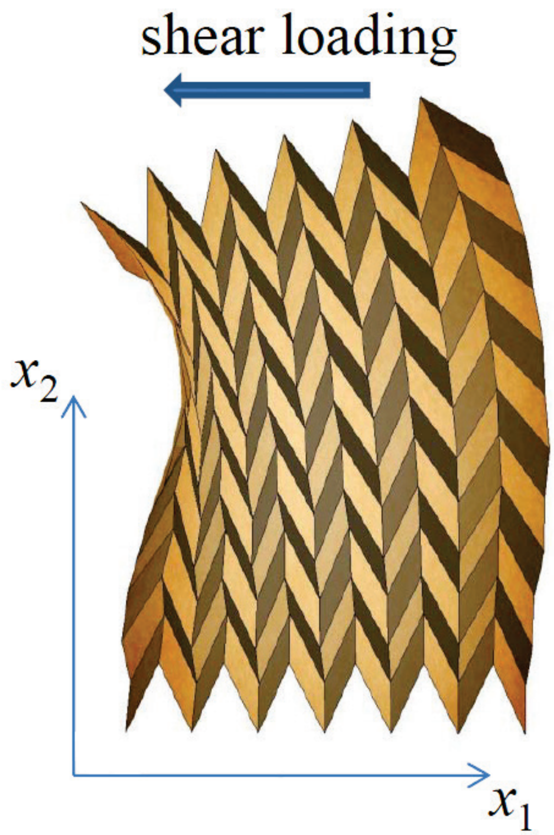

Supplementary Figure S4. Shear deformation of a Miura-ori. Deformation of a (13,13) Miura-ori under shear loading along the negative x_1 direction. It is observed that the opposite relationship between shear loading and shear deformation.

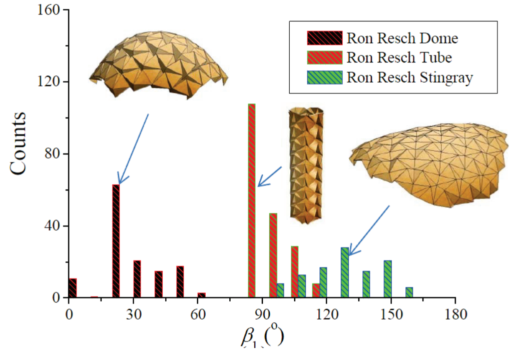

(a)

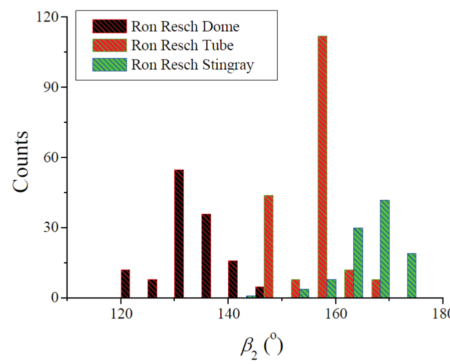

(b)

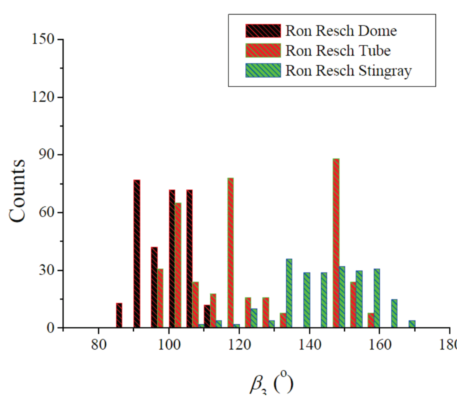

(c)

Supplementary Figure S5. Histograms of the three dihedral angles (a) β_1, **(b)** β_2, and **(c)** β_3 for three Ron Resch patterns, namely a Ron Resch dome, a tube and a stingray.

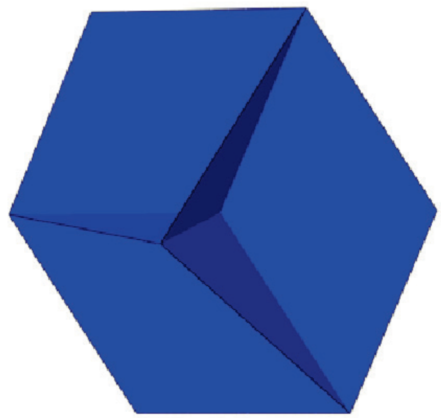

(a)

(b)

Supplementary Figure S6. Unit cell for buckling analysis. (a) Completed collapsed Ron Resch plate. **(b)** Six-fold supporting structure.

References

1. B. Liu, Y. Huang, H. Jiang, S. Qu, K. C. Hwang, *Computer Methods in Applied Mechanics and Engineering* **193**, 1849 (2004).
2. B. Liu *et al.*, *Physical Review B* **72**, 8 (Jul, 2005).